IOP Publishing Biomed. Mater. **19** (2024) 025010 https://doi.org/10.1088/1748-605X/ad1d7f

Biomedical Materials

OPEN ACCESS

RECEIVED
14 October 2023

REVISED
19 December 2023

ACCEPTED FOR PUBLICATION
11 January 2024

PUBLISHED
22 January 2024

PAPER

In vitro analysis of insoluble salt formation mechanism associated with Mg corrosion—variations depending on the diffusion environment in model tissue

Masanobu Hayashi[1,*], **Akiko Yamamoto**[2], **Takayuki Aizawa**[3], **Yu Yusa**[1], **Yoshinaka Shimizu**[1,4] **and Yoshimichi Imai**[1]

[1] Department of Plastic and Reconstructive Surgery, Tohoku University Graduate School of Medicine, 2-1 Seiryo-machi, Aoba-ku, Sendai, Miyagi 980-8575, Japan
[2] Research Center for Macromolecule and Biomaterials, National Institute for Materials Science, 1-1 Namiki, Tsukuba, Ibaraki 305-0044, Japan
[3] Department of Plastic and Reconstructive Surgery, Tohoku Kosai Hospital, 2-3-11 Kokubunmachi, Aoba-ku, Sendai, Miyagi 980-0803, Japan
[4] Nihon Parkerizing Co., Ltd, 1-15-1, Nihonbashi, Chuo-ku, Tokyo 103-0027, Japan
[*] Author to whom any correspondence should be addressed.

E-mail: snhrr116@yahoo.co.jp

Keywords: magnesium, *in vitro* model tissue, corrosion, insoluble salt precipitation, Raman spectroscopy

Supplementary material for this article is available online

Abstract

Magnesium (Mg) alloys have attracted attention as biodegradable metals, but the details of their corrosion behavior under biological environment have not been elucidated. Previous studies have suggested that diffusion through blood flow may influence Mg corrosion. Therefore, to understand the degradation behaviors of Mg, we analyzed insoluble salt precipitation associated with Mg corrosion in model tissue with different diffusion rates. A pure Mg specimen was immersed into a model tissue prepared with cell culture medium supplemented by a thickener at a different concentration (0.2%–0.5%) to form the gel. Micro-focus x-ray computed tomography of the gel was performed to observe gas cavity formation around the specimen. The insoluble salt layer formed on the specimen surface were analyzed by scanning electron microscopy with energy-dispersive x-ray spectroscopy, and Raman spectroscopy. As results, gas cavity formation was observed for all specimens. At day 7, the gas cavity volume was the highest at 0.5% thickener gel followed by 0.3% thickener gel. The insoluble salts were classified into three types based on their morphology; plate-like, granular-like, and crater-like salts. The crater-like salts were observed to cover 16.8 ± 3.9% of the specimen surface immersed in the 0.5% thickener gel, at the specimen area contacted to the gas cavity. The crater-like salts were composed by Mg hydroxide and carbonate from the deepest to the top layer. In plate-like or granular-like salts, Mg carbonate was formed in the deepest layer, but phosphates and carbonates, mainly containing calcium not Mg, were formed on the surface layer. In conclusion, the increase in the thickener concentration increased the gas cavity volume contacting to the specimen surface, resulting in the increase in precipitation of Mg hydroxide and carbonate, composing crater-like salts. Mg hydroxide and carbonate precipitation suggests the local increase in OH^- concentration, which may be attributed to the decrease in diffusion rate.

1. Introduction

Titanium (Ti) and biodegradable polymers are commonly employed in the osteosynthesis implants for treating bone fractures. Although Ti has excellent mechanical strength, corrosion resistance, and biocompatibility [1, 2], it can remain as a foreign body even after healing of the bone fracture, leading to adverse effects and subsequent surgical removal as an ultimate solution [3, 4]. On the other hand, biodegradable polymers such as poly-L-lactic acid can avoid this issue, but they have low mechanical strength, which limits their application to the areas with strong load-bearing [5]. In the past decade, magnesium (Mg) alloys have attracted attention of medical doctors and researchers as new materials for osteosynthesis implants. Since Mg alloys are easily corroded by reacting with water in body fluids, they can degrade and disappear within the body after healing, which makes them ideal bone-fixation materials. Mg is an essential element for human metabolism, therefore released ions are expected to have low toxicity for humans. Furthermore, Mg and its alloys have a Young's modulus similar to that of the human cortical bone, that is advantageous for bone-jointed materials [6]. Recently Mg alloy screws have widely used in clinical cases, but its corrosion reaction causes gas cavity formation in the tissue, thereby retarding the healing process of the damaged tissue [7]. In order to identify the causes of adverse events associated with the degradation of Mg, it is necessary to understand the degradation behavior of Mg. For the success of clinical application, it is important to clarify following aspects including corrosion rate, reduction in the device strength, formation of gas cavities, precipitation of insoluble salts, and their effects on the surrounding tissues. However, the *in vivo* degradation behavior of Mg alloy is yet to be elucidated as its corrosion rate differs depending on the implanted tissue [8–10]. The blood flow in tissues can be one of the important factors that promotes Mg alloy corrosion [8–11]. Fluid circulation by capillary system is mainly responsible for ion and gas diffusion in the tissue, resulting in differences in local Mg^{2+}, OH^-, and H_2 distributions. This can change the behavior of the insoluble salt formation on the Mg alloy surface, thereby influencing the corrosion rate of the Mg alloy and the healing process of the surrounding tissue.

Based on the background described above, in this study, we simulated different fluid circulation environments by preparing model tissues with different ion and gas diffusion rates. We conducted immersion tests of pure Mg specimens into these model tissues under a simulated *in vivo* environment (37 °C, 5% CO_2, >95% relative humidity) to investigate the gas cavity formation in the model issues and analyze the insoluble salt formation on the specimen surface.

The aim of this study it to understand the effect of diffusion rate in the tissue on the insoluble salt formation behavior of pure Mg.

2. Methods

2.1. Test materials

A commercially available 99.9% Mg wire (φ1 mm; MACRW Co., Ltd) was cut into 6 mm in length and polished to JIS #2500 using SiC paper and routing. The nominal composition of the Mg wire is provided in table 1. The natural oxide film on the specimen surface was removed by immersion in a nital solution (5% nitric acid in ethanol) at 20 °C, and the specimen was washed with ultrapure water before drying under vacuum [12, 13]. The Mg specimen was sterilized with ethylene oxide gas prior to the immersion test.

2.2. Immersion in model tissue

Figure 1 displays the concept of the model tissue employed in the present study. A polysaccharide, gellan gum (FUJIFILM Wako Chemicals) was added to the simulated body fluid as a thickener to form a gel as an immersion medium [14]. In this experiment, three types of the gel were prepared with different thickener concentrations; 0.2%, 0.3%, and 0.5%. These concentrations were selected based on our previous paper reporting 0.4% thickener concentration [14]. A pre-test revealed the thickener concentration of 0.2% as the lowest limit to hold the Mg sample in the gel. Consequently, concentrations of 0.2%, 0.3%, and 0.5% were designated to represent high, medium, and low diffusion environments, respectively. Eagle's minimum essential medium (E-MEM, 'Nissui' 1, Nissui Pharmaceutical Co., Ltd) supplemented with newborn bovine serum was used as a simulated body fluid. The major chemical components of E-MEM are shown in table 2.

After the preparation of the model tissue solution following the procedure in [14], a 6 ml portion of it was dispensed into a sterilized container and solidified at room temperature (20 °C–25 °C) for about 3 min. Then, the Mg specimen was inserted into the model tissue. Thereafter, 2 ml of the model tissue solution was dispensed over and solidified at 20 °C–25 °C for extra 3 min. Subsequently, the model tissue with the Mg specimen was placed in a CO_2 incubator with the container lid loosened. All experiments were performed aseptically in a clean cabinet to avoid contamination, and the experiment was performed in triplicate at each concentration of the thickener.

2.3. Micro-focus x-ray computed tomography observation

The micro-focus x-ray computed tomography (µCT, SMX-90CT, Shimadzu Corporation) of the model tissue with the Mg specimen was performed on 0, 1, 3, 5, and 7 d of the immersion at the optimum condition (110 µA and 90 kV) with the resolution of 21 µm $voxel^{-1}$. A three-dimensional (3D) image of the gas cavity distribution was created using an image analysis software (VG Studio Max ver. 2.0, Volume Graphics GmbH). The initial surface area was decided based on the µCT image at day 0.

After 7 d of immersion, Mg specimen was collected from the model tissue and vacuum dried. Then, the specimen was observed by µCT with the higher resolution of 7 µm $voxel^{-1}$.

Table 1. Composition of the pure Mg wire (mass%).

	Al	Mn	Zn	Si	Cu	Ni	Fe	Mg
Mg sample	0.009	0.011	0.016	0.003	0.008	0.001	0.002	Bal.

Bal.: balance.

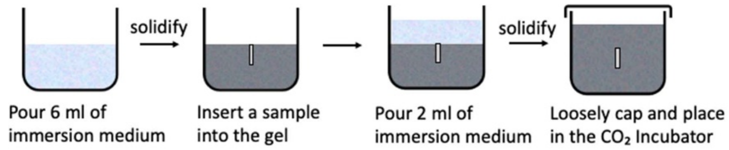

Figure 1. Schematic illustration of the implantation procedure in the model tissue.

Table 2. Major chemical components of E-MEM.

Component	E-MEM
Na^+ (mM)	143.5
K^+ (mM)	5.37
Mg^{2+} (mM)	0.81
Ca^{2+} (mM)	1.8
Cl^- (mM)	124.7
$HCO_3{}^-$ (mM)	26.2
$HPO_4{}^{2-}$ (mM)	0.9
$SO_4{}^{2-}$ (mM)	0.81
Glucose ($g\,l^{-1}$)	1
Amino acids and vitamins ($g\,l^{-1}$)	0.81
Phenol red ($g\,l^{-1}$)	0.006

2.4. Analysis of insoluble salts by scanning electron microscopy with energy-disperse x-ray spectroscopy

The surfaces and longitudinal sections of the before and after immersed specimens were analyzed using a scanning electron microscope equipped with energy dispersive x-ray spectroscopy (SEM-EDX, S-4800, Hitachi High-Technologies Co., Ltd). The specimen was embedded in a methyl methacrylate resin, and then, cut along its longitudinal direction. In prior to the SEM observation, the specimen surface was coated by Pt. Elemental analysis was performed at an acceleration voltage of 15 keV.

2.5. Analysis of insoluble salts by micro-Raman spectroscopy

The surfaces and longitudinal sections of the immersed specimens were analyzed by Raman spectroscopy (NRS-5100, JASCO Co., Ltd). The measurement conditions were as follows; grating $L = 600$ nm, $B = 500$ nm, objective lens magnification = 100, excitation laser = 532.13 nm, exposure time = 10 s, number of integrations = 5 times, laser power = 3.2 mW (50% in measurement), and wave number range = 100–3700 cm^{-1}.

3. Result

3.1. Surface and cross-sectional analysis of the immersed specimens by SEM-EDX

3.1.1. Morphological and elemental analysis of the specimen surface by SEM-EDX

Figure 2 indicates the examples of the macroscopic images of the specimen in the model tissue during the 7 d of immersion. The gas cavity formation was observed for all specimens immersed into the model tissue. The macroscopic images clearly show the difference in the gas cavity volume and distribution in the model tissue with different thickener concentrations; the larger total gas cavity volume was observed in the model tissue with the highest thickener concentration (=the lowest diffusion rate). The growth of the gas cavity is more obvious in the model tissue with the higher thickener concentration than that with the lower thickener concentration (supplemental figure S1). The gas cavity volume at day 7 was 3.49 ± 0.45, 4.04 ± 0.20, 4.78 ± 0.08 $mm^3\ mm^{-2}$ for the model tissue with 0.2%, 0.3%, and 0.5% thickener concentrations, respectively.

Figure 3 shows examples of optical microscope and SEM images of the specimen surface before and after immersion in the model tissue. Localized precipitation of insoluble salts was observed on the all specimens with differences in their morphology and distribution between the different thickener concentrations. Precipitates were classified into three types: a crater-shaped deposits, smooth plate-like structure distributed over a wide area, and a cluster of granular precipitates formed on smooth structure. These salts are called as crater-, granular-, and plate-like salts, respectively. Typical magnified images of these salts are shown in figure 4.

Table 3 summarizes the distribution of each type of the salts. First, the crater-like salt was widely distributed on the specimen of the 0.5% group, the highest thickener concentration. As the thickener concentration decreased, the distribution of the

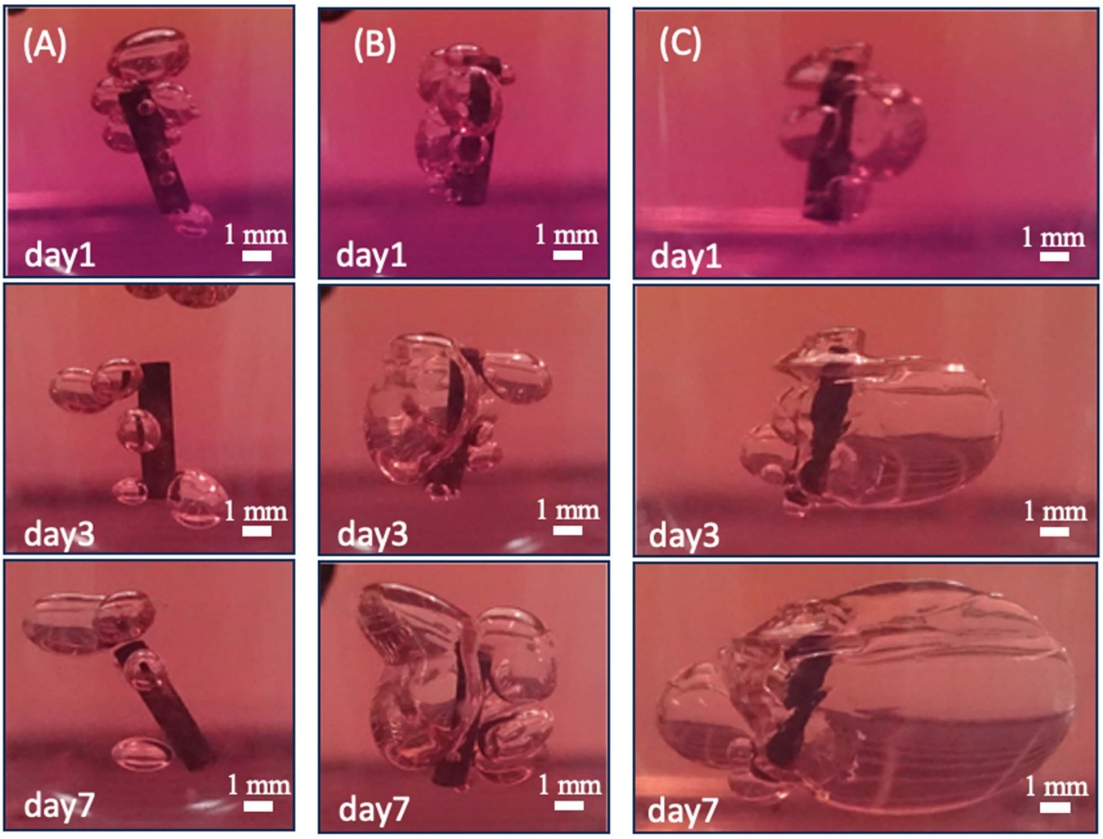

Figure 2. Macroscopic images of the Mg specimen in the model tissue at day 1, 3, and 7 with the thickener concentrations of 0.2% (A), 0.3% (B), and 0.5% (C).

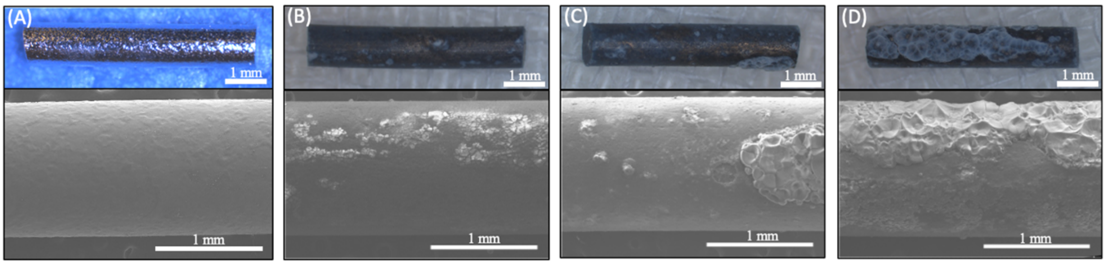

Figure 3. Macroscopic (top) and SEM (bottom) images of Mg specimen surfaces before immersion (A) and after immersion in model tissue with thickener concentrations of 0.2% (B), 0.3% (C), and 0.5% (D).

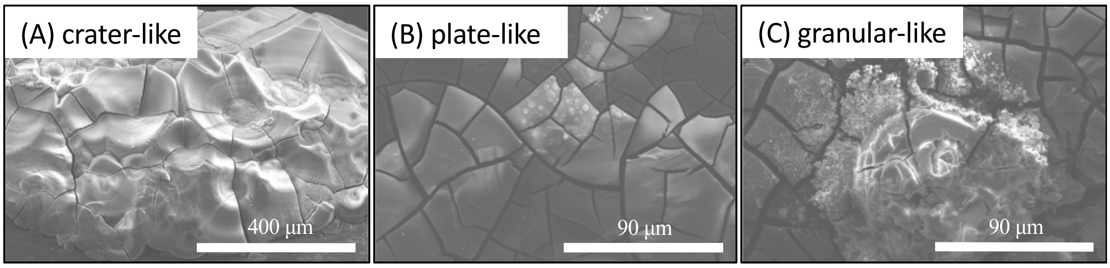

Figure 4. Typical SEM images of the insoluble salts classified by their morphology as crater-like (A), plate-like (B), and granular-like (D) salts.

Table 3. Trend of insoluble salt distribution on the Mg specimen surface immersed in the model tissue.

	Thickener concentration		
Salt morphology	0.2%	0.3%	0.5%
Crater-like	−	±	++
Plate-like	+	+	+
Granular-like	+	+	±

crater-like salt decreased; it was not observed at all in the 0.2% group. In the granular-like salt, an aggregation of small clusters was observed on the specimen in the 0.2% group. The distribution of the granular-like salt decreased as the thickener concentration increased; it was hardly observed in the 0.5% group. The plate-like salt was widely distributed on the specimen in all groups.

The results of the elemental analysis of the specimen surface before immersion is shown in figure 5. No insoluble salt was observed on the specimen surface before immersion, and SEM-EDX chart displayed a dominant peak derived from Mg.

Figures 6–8 displays the results of SEM-EDX analysis of the insoluble salts formed on the immersed specimen surface, and the detected elements are summarized in table 4. The crater-like salts observed in the 0.3% and 0.5% groups had similar morphologies and contained Mg/O/C. In plate-like salts, Mg/Ca/P/O/C was detected in all groups. In the granular-like salt, Ca/Mg/P/O/C was detected. These results suggest that the crater-like salt is an Mg salt, and the granular- and plate-like slats are mixture of Mg and calcium (Ca) salts.

3.1.2. Cross-sectional elemental analysis by SEM-EDX

The results of elemental analysis on the longitudinal sections of the specimen are shown in figure 9 and table 5. An insoluble salt layer with a thickness of approximately 20–40 µm was observed at the deposited area of plate- and granular-like salts. Common changes were observed in the elemental distribution along the cross-section: Mg/C/O in the deepest layer, Mg/P/C/O in the middle layer, and Ca/Mg/P/C/O in the surface layer of the insoluble salts.

A similar analysis was performed on the deposited area of the crater-like salt of the specimen in the 0.5% group. The insoluble salt layer was thick as 50−120 µm, unlike other types of salts. The crater-like salt had an elemental distribution of Mg/C/O from the deepest to the surface layers. Based on these data, followings are estimated: Ca phosphates were precipitated near the surface layer in the plate-like and granular-like salts. Mg phosphates and carbonates were precipitated in the middle layer of these types of salts. Mg carbonates and hydroxides were precipitated in the deep layers of these types of salts as well as in the crater-like salt.

3.2. Analysis of the insoluble salts by micro-Raman spectroscopy

3.2.1. Surface analysis by micro-Raman spectroscopy

The Raman spectra of insoluble salts formed on the specimens immersed in the model tissue are presented in figure 10 and table 6. The crater-like salt showed peaks at 1120 and 3561 cm^{-1}. The plate-like salt showed peaks at 1092 and 2930 cm^{-1}, and the spectrum was similar in each group. The peaks of granular-like salt of the 0.2% group were observed at 946, 1090, and 2948 cm^{-1}.

3.2.2. Cross-sectional analysis by micro-Raman spectroscopy

Figure 11 and table 7 show the results of the micro-Raman spectroscopy along the cross-section of the specimens immersed in the model tissue with 0.5% or 0.2% thickener concentration. For the reference, figure 12 shows the Raman spectrum of the cross-section of the Mg specimen before immersion. In all groups, the spectrum of the deepest layer shows the waveform of the Mg specimen before the immersion. In the deposited area of granular- and plate-like salts, a peak at the Raman shift of 1090 cm^{-1} was detected from the deepest to the surface layers. Other peaks were observed at 946 and 2948 cm^{-1} in the shallow and surface layers. In addition to these, peaks at 825 and 1340 cm^{-1} were clearly observed in the shallow and surface layers in the 0.2% group. In all thickener concentrations, the tendency in the change of the Raman spectrum from the deepest to the surface layer was consistent, but peaks were more distinct in the 0.2% group, suggesting the progress in precipitation of insoluble salts. At the cross section of the deposited area of crater-like salt in the 0.5% group, steep peaks were observed at 1120 and 3561 cm^{-1} with no change in the Raman spectrum from the deepest to the surface layer.

3.3. µCT 3D images of the gas cavity and the specimen

The examples of the 3D-images of the gas cavity distribution around the specimen in the model tissue and the specimen surface after 7 d of immersion are shown in figure 13. The optical microscopic images of the insoluble salt on the specimen surface were compared to those of the µCT images as well. The distributed area of the crater-like salts corresponds with the specimen area contacted to the gas cavity. Table 8 presents the ratio of surface area in contact with the gas cavity and that of the region of crater-like salt precipitation based on µCT and optical microscopic images. The ratio of gas cavity contact area increased

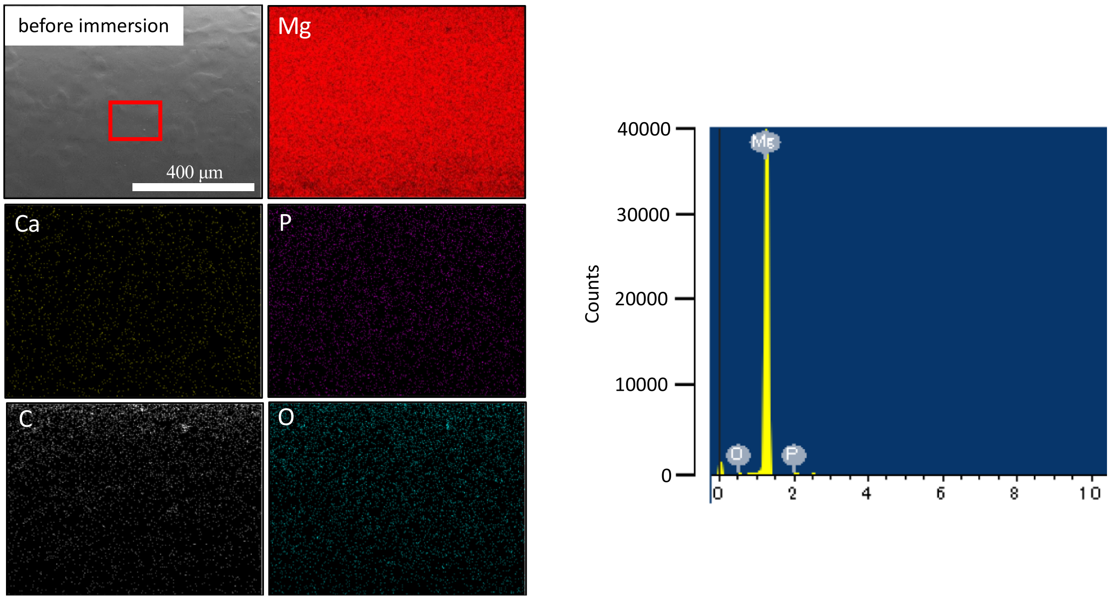

Figure 5. EDX analysis of the Mg specimen surface before immersion. Elemental mapping (left) and EDX spectra (right) of the point analysis shown in the SEM micrograph as □.

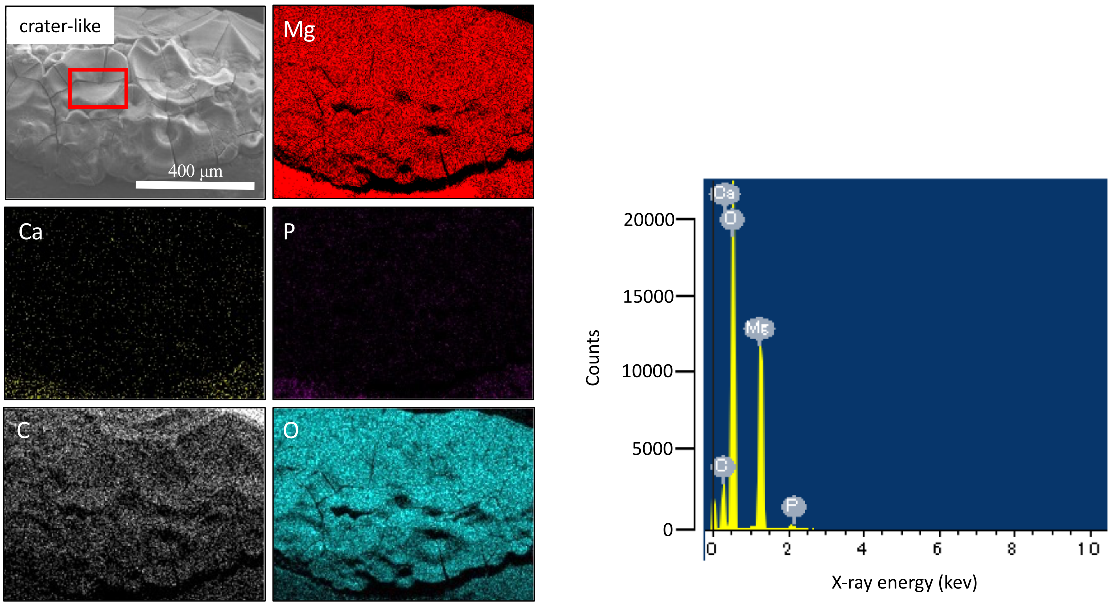

Figure 6. EDX analysis of the crater-like salt formed on the Mg specimen immersed in the model tissue with 0.5% thickener. Elemental mapping (left) and EDX spectra (right) of the point analysis shown in the SEM micrograph as □.

with increase in thickener concentration, as well as those of the crater-like salt region.

4. Discussion

The *in vivo* corrosion of Mg involves many factors, including inorganic salts and proteins contained in a body fluid, pH, and body fluid circulation. According to previous reports, immediately after implantation, Mg reacts with water to be corroded, releasing Mg^{2+}, OH^- and H_2 gas [15]. In case of the immersion in water, local concentrations of Mg^{2+} and OH^- increase and eventually exceed their solubility limit, resulting in the precipitation of $Mg(OH)_2$ on the Mg surface. This insoluble salt layer formation interferes the direct contact between Mg and water, retarding the corrosion rate. In an *in vivo* environment, a body fluid such as blood plasma has a buffering capacity and is maintained at pH 7.4 [16]. Therefore, if the diffusion by the blood flow is sufficient, the increase in the local concentrations of Mg^{2+} and OH^- is suppressed, resulting in the no precipitation of $Mg(OH)_2$. However, the blood plasma and interstitial fluid contain carbonic and phosphoric acids, which easily form insoluble salts. Carbonic and phosphoric acids are polyprotic acids, possible

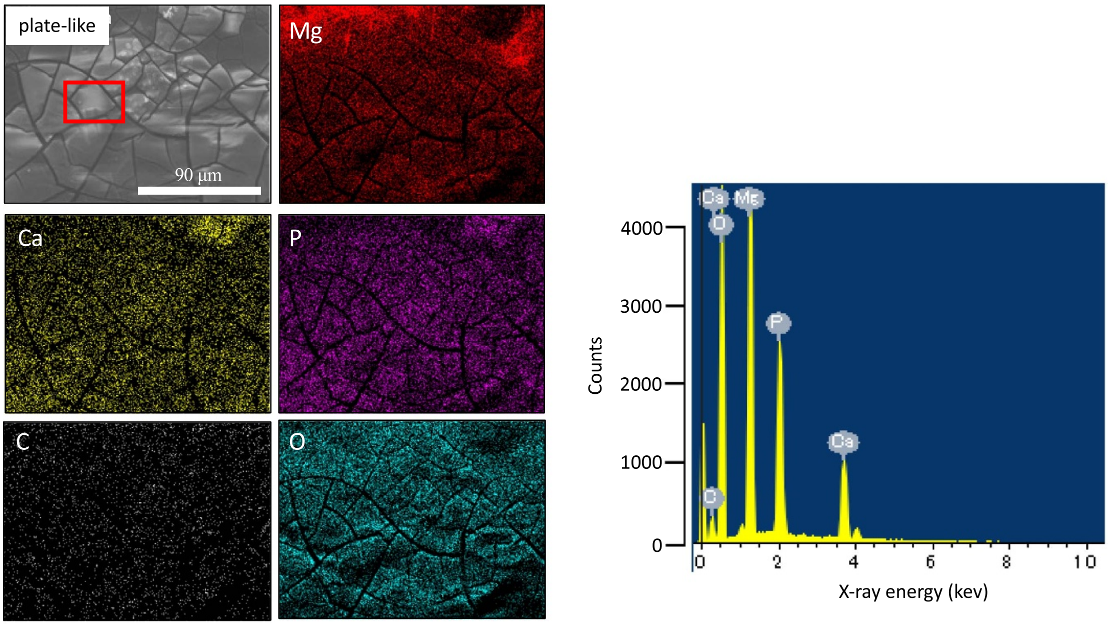

Figure 7. EDX analysis of the plate-like salt formed on the Mg specimen immersed in the model tissue with 0.5% thickener. Elemental mapping (left) and EDX spectra (right) of the point analysis shown in the SEM micrograph as ☐.

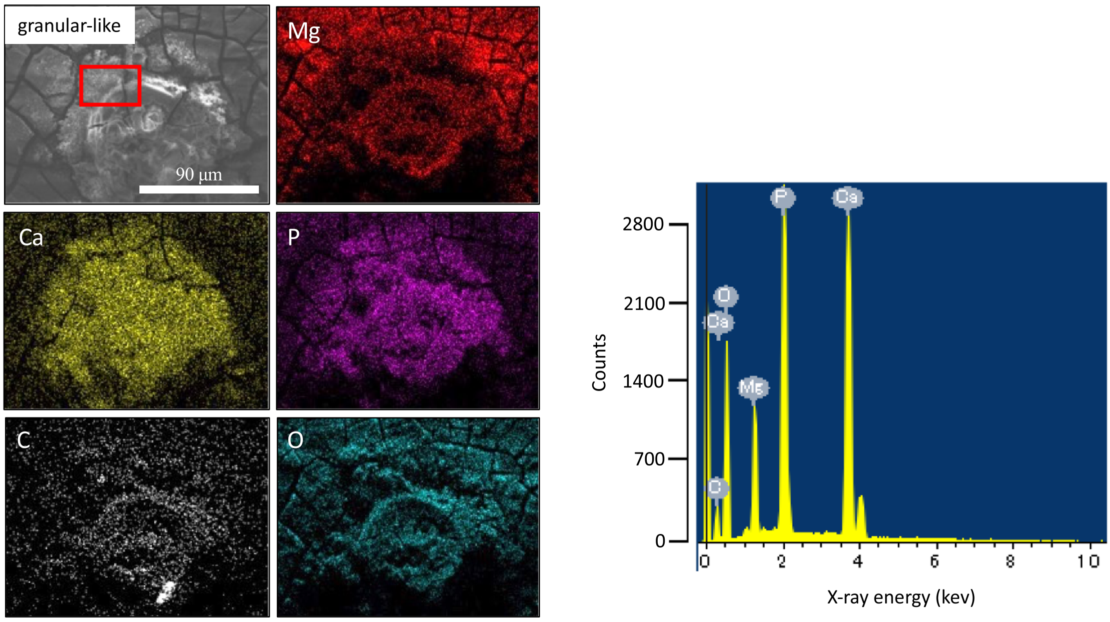

Figure 8. EDX analysis of the granular-like salt formed on the Mg specimen immersed in the model tissue with 0.2% thickener. Elemental mapping (left) and EDX spectra (right) of the point analysis shown in the SEM micrograph as ☐.

Table 4. Elemental distribution in the insoluble salts formed on the Mg specimen surface immersed in the model tissue.

	Thickener concentration		
Salt morphology	0.2%	0.3%	0.5%
Crater-like	—	Mg/O/C	Mg/O/C
Plate-like	Mg/Ca/P/O/C	Mg/Ca/P/O/C	Mg/Ca/P/O/C
Granular-like	Ca/Mg/P/O/C	Ca/Mg/P/O/C	—

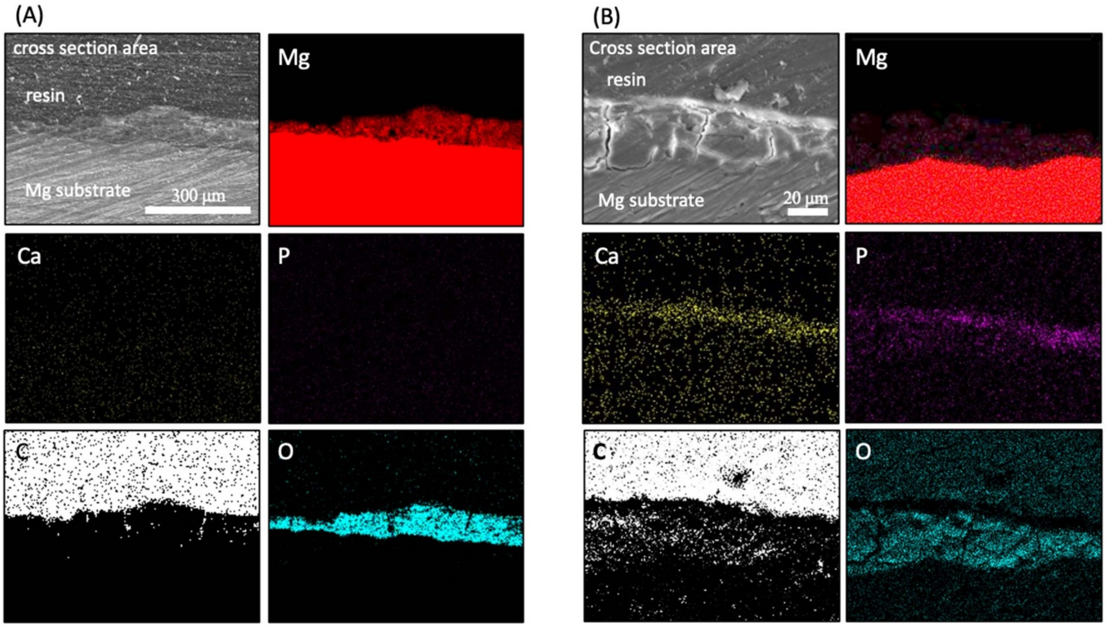

Figure 9. Cross-sectional EDX analysis of crater-like (A) and plate-like (B) salts formed on the Mg specimen immersed in the model tissue with 0.5% (A) and 0.2% (B) thickener concentrations.

Table 5. Cross-sectional analysis of elemental distribution in insoluble salts on the Mg specimen immersed in the model tissue.

Position in the cross section	Salt morphology	
	Crater-like	Plate-, granular-like
Superficial	Mg/O/C	Ca/P/O/C
Middle	Mg/O/C	Mg/P/O/C
Deepest	Mg/O/C	Mg/O/C

to have different dissociation states (e.g., carbonic acid as H_2CO_3, HCO_3^{-3} and CO_3^{2-}, and phosphoric acid as H_3PO_4, $H_2PO_4{}^-$, HPO_4^{2-}, and PO_4^{3-}) in an equilibrium. The concentrations of the polyvalent anions such as CO_3^{2-}, HPO_4^{2-}, and PO_4^{3-} increase when OH^- is increased by the Mg corrosion reaction. Therefore, the salts of Mg^{2+} (released) and Ca^{2+} (in the body fluid) may precipitate by exceeding their solubility limits. Table 9 lists the allowable concentrations of Mg^{2+} and Ca^{2+} (maximum concentration without precipitation) calculated for the phosphates, carbonates, and hydroxide [17]. Phosphate is most likely to precipitate in E-MEM, whereas the precipitation of hydroxide requires an increase in OH^- and Mg^{2+} concentrations more than ten times of those of phosphate and carbonate. In addition, Mg^{2+} and Ca^{2+} are competitive in the phosphate and carbonate formation [18], but Ca salts are more likely to precipitate in the body fluid. The Ca^{2+} concentration in E-MEM (1.8×10^{-3} M) is oversaturated for the solubility of $Ca_3(PO_4)_2$. These calculations about solubility limits clearly indicate the possibility of the diffusion in the corrosion environment to influence the composition of insoluble salts precipitated on the Mg surface through the changes in local ion concentrations near the Mg surface. In addition, the precipitation behavior of insoluble salts affects Mg corrosion rate because insoluble salts prevent contact of the underlying metal Mg to water, resulting in the suppression of the corrosion reaction.

Optical microscopy and SEM observations indicate that the diffusion ability of the model tissue influences the morphology and composition of insoluble salts precipitated on the specimen surface. The precipitation of granular-like salt was widespread in the 0.2% group, which had a higher diffusion ability. A crater-like salt was observed in both the 0.5% and 0.3% groups but was more common in the 0.5%, which had the lowest diffusion ability. From the results of the SEM-EDX analysis, it was assumed that the crater-like salt was an Mg salt, granular-like salt was a Ca salt, and plate-like salt was a double salt or a mixture of Mg and Ca salts. Table 6 indicates the results of micro-Raman spectroscopy: peaks at 1120 and 3656 cm^{-1} for the crater-like salt, 1092 and 2930 cm^{-1} for plate-like salt, and 946, 1090 and 2948 cm^{-1} for granular-like salt. The peak at 946 cm^{-1} is assigned to the v_1 stretching vibration of P—O [19–21] whereas those at 1092, 1120 cm^{-1} is to stretching vibration of CO_3^{2-} [22–24]. The peak at 2930 cm^{-1} is assigned to the stretching vibration of $-CH_3$ in an organic component such as protein [25, 26], and the peak at 3600 cm^{-1} is assigned to the stretching vibration of $-OH$ [24, 27]. Therefore, the crater-like salt contains Mg hydroxide and carbonate,

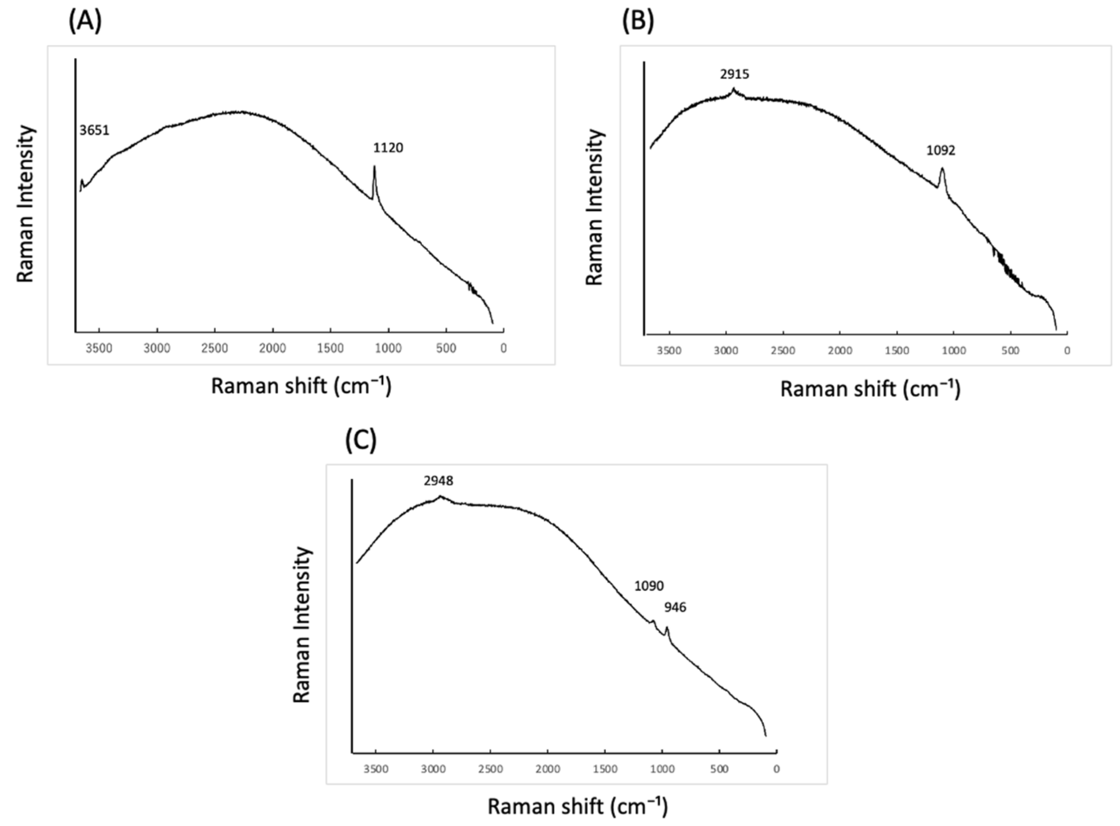

Figure 10. Typical Raman spectra of insoluble salts formed on the Mg specimen immersed in the model tissue as (A) crater-, (B) plate-, and (C) granular-like salts.

Table 6. Raman shifts of the major peaks observed for the insoluble salts formed on the Mg specimen surface immersed in the model tissue (cm^{-1}).

	Thickener concentration		
Salt morphology	0.2%	0.3%	0.5%
Crater-like	—	3630, 1120	3651, 1120
Plate-like	2915, 1092	2935, 1092	2930, 1092
Granular-like	2948, 1090, 946	2952, 1095, 947	—

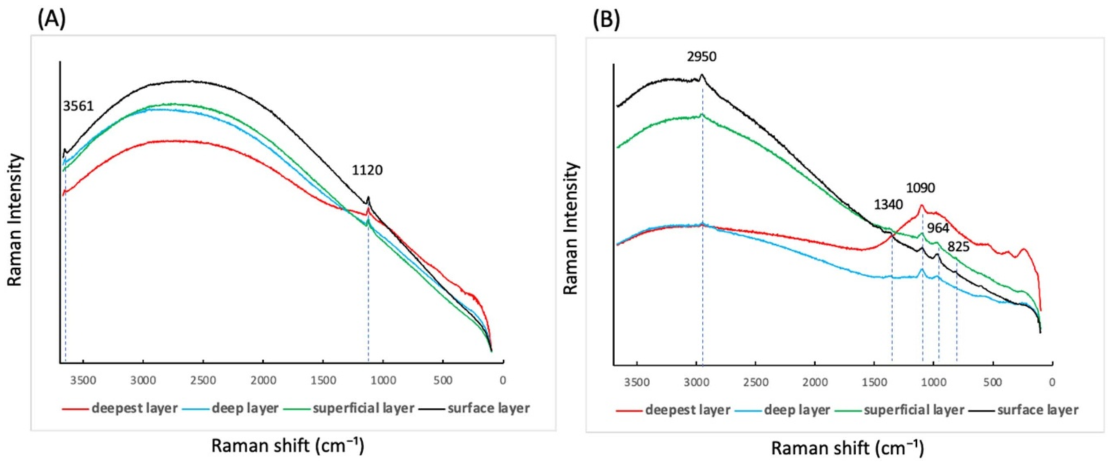

Figure 11. Cross-sectional Raman spectra of the (A) crater- and (B) granular-/plate-like insoluble salts formed on the Mg specimen immersed in the model tissue with (A) 0.5% and (B) 0.2% thickener concentrations.

Table 7. Raman shifts of the major peaks observed for the cross section of insoluble salt layer (cm^{-1}).

Position in the cross section	Thickener concentration			
	0.2%	0.3%	0.5%	0.5% (Crater-like)
Surface	2950, 1340, 1090, 964, 825	2948, 1090, 964	2948, 1090, 946	3561, 1120
Shallow	2950, 1340, 1090, 964	2948, 1090, 946	2948, 1090	3561, 1120
Deep	2950, 1090, 964,	2948, 1090	2948, 1090	3561, 1120
Deepest	1090	1090	1090	3561, 1120

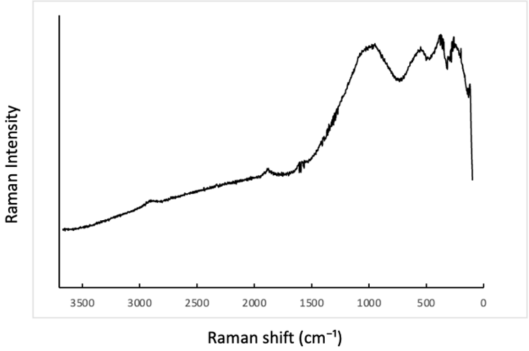

Figure 12. Raman spectrum of the cross-section of an un-used Mg specimen.

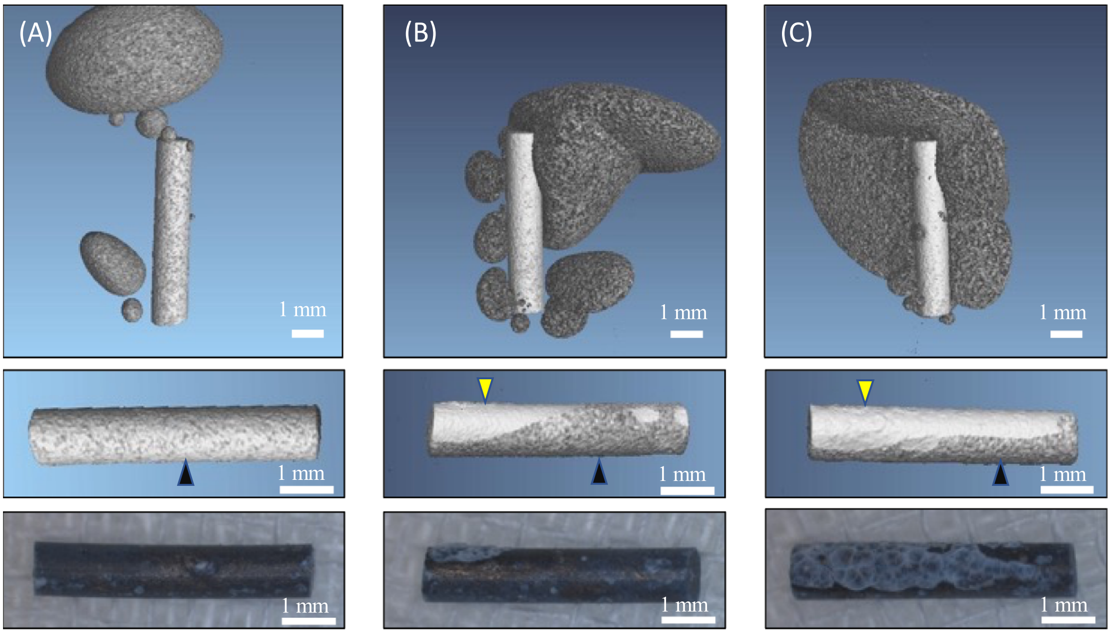

Figure 13. Three dimensional images of the gas cavity and the specimen in the model tissue (top), specimen after immersion (middle), and optical microscopic images of the specimen after immersion (bottom) in the model tissue with (A) 0.2 %, (B) 0.3 %, and (C) 0.5% thickener concentration. Scale bar: 1 mm. Yellow and black arrowheads indicate the specimen area in contact with the gas cavity and the model tissue, respectively.

the plate-like salt does Mg and Ca carbonates and phosphates, and the granular-like salt does Ca carbonates and phosphates. Mg and Ca carbonates and phosphates have high affinity to organic components. Therefore, the peak assigned to $-CH_3$ in Raman spectroscopy can be derived from the presence of organic components on the surface of these salts, either adsorbed or co-precipitated [28, 29].

The cross-sectional SEM-EDX analysis of the plate-like insoluble salt layer reveals that Mg distribution tends to be high in deep layers and low in shallow layers, while Ca distribution is not observed in deep layers and tends to be high in shallow layers (table 5). Combined with the Raman spectroscopy results (table 7), the deepest layer contains magnesium carbonate, and the deeper to shallower

Table 8. Ratio of the specimen surface area contact with the gas cavity and the region of crater-like salt precipitation to total surface area (%).

	Thickener concentration		
Area percentage	0.2%	0.3%	0.5%
Contact area with gas cavity	0 ± 0	13.7 ± 3.2	38.8 ± 6.6
Crater-like salt coverage	0 ± 0	2.2 ± 3.1	16.8 ± 3.9

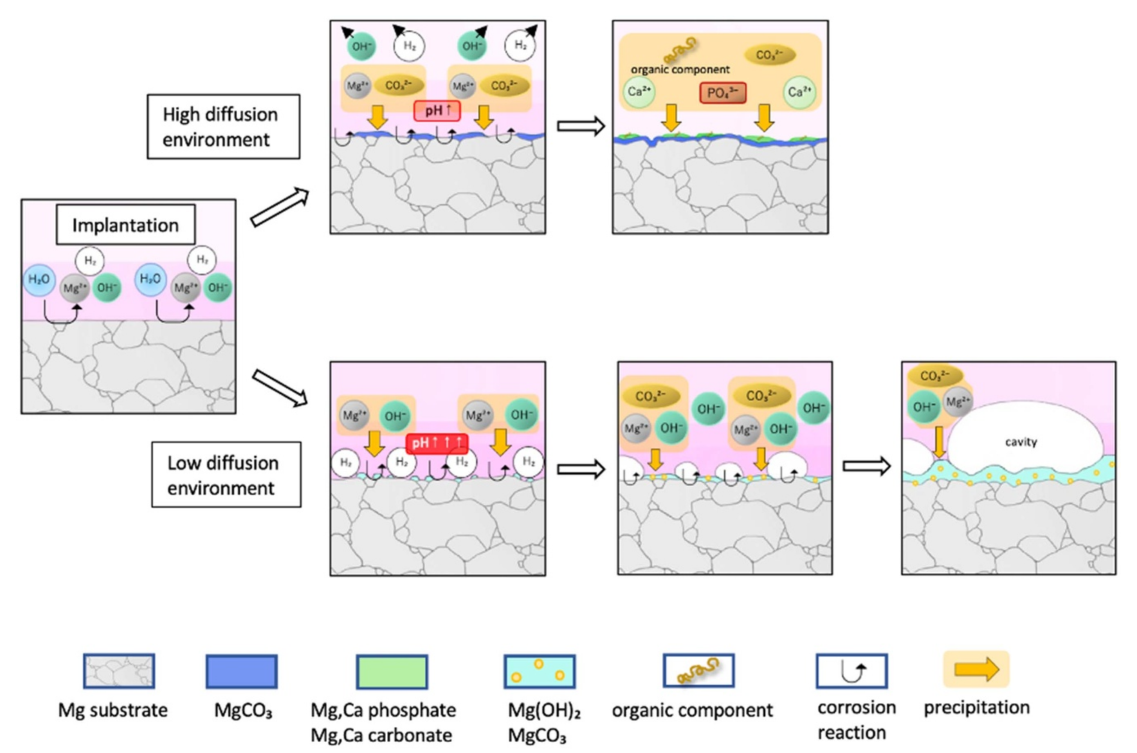

Figure 14. Schematic illustration of insoluble salt formation mechanism depending on the diffusion environment.

Table 9. Solubility product (K_{sp}) of insoluble salts and maximum allowable concentration of cations at different pH conditions.

Salt	K_{sp}[a]	Anion concentration in E-MEM (pH 7.4)[b] ($\mathrm{mol\,l^{-1}}$)	Maximum allowable concentration of cation ($\mathrm{mol\,l^{-1}}$) pH 7.4	pH 8.5
$Mg(OH)_2$	5.61×10^{-12}	2.51×10^{-7}	8.89×10^{3}	5.61×10^{1}
$MgCO_3$	6.82×10^{-6}	3.77×10^{-4}	2.43×10^{-1}	1.81×10^{-2}
$CaCO_3$	3.36×10^{-9}	3.77×10^{-4}	1.20×10^{-4}	8.92×10^{-6}
$Mg_3(PO_4)_2$	1.04×10^{-24}	1.29×10^{-7}	2.89×10^{-3}	3.96×10^{-4}
$Ca_3(PO_4)_2$	2.07×10^{-33}	1.29×10^{-7}	3.64×10^{-6}	4.99×10^{-7}

[a] at 25 °C in pure water.

[b] Concentrations of target ion species calculated based on the dissociation constants of carbonic and phosphoric acids. Details are given in [17].

layers contain Mg carbonate, Ca carbonate, and phosphate. The shallow to surface layers predominantly contain Ca carbonate and Ca phosphate. As mentioned earlier, Mg and Ca carbonates and phosphates can contain organic components through adsorption and/or co-precipitation. These results suggest that the plate-like salt has a layered structure of Mg and Ca carbonates and phosphates, while the granular salt corresponds to Ca carbonates and phosphates. Conversely, the cross-sectional analysis of the crater-like insoluble salt layer shows that from the deepest layer to the surface layer, Mg hydroxide and Mg carbonate are present with no stratification change. The peak corresponding to the stretching vibration of −OH in hydroxide was observed only in the crater-like salt. The different structure of the crater-like salt from those of the plate- and granular-like salts suggests a difference in the corrosion environment.

Figure 13 and table 8 reveal a correlation in the ratio between the specimen surface area in contact with the gas cavity and the occurrence of crater-like salt precipitation. Variations in the ion and gas diffusion capacities of the model tissue also influence the formation of gas cavities. The presence of thickener molecules reduces the ion and gas diffusion rate in the model tissue [30]. If the diffusion of H_2 in tissue is lower than the H_2 generation by Mg corrosion, H_2 accumulates in the tissue, leading to the formation of a gas cavity [14]. Consequently, the gas cavity volume in the model tissue increases with an elevation in thickener concentration, signifying a reduced gas diffusion rate in the tissue. On the specimen surface in contact with the gas cavity, there is no diffusion into the tissue, nor is there a supply of Ca^{2+} and phosphate from the body fluid. As a result, Mg hydroxide and carbonate become the primary components of the insoluble salts, with no precipitation of phosphates. The lower diffusion rate in the model tissue promotes gas cavity formation, hindering contact between the specimen surface and the tissue, thus further diminishing diffusion. This will cause differences in the corrosion behavior of the Mg specimen and insoluble salt formation on its surface. This will cause differences in the corrosion behavior of the Mg specimen and insoluble salt formation on its surface. In the present study, crater-shaped salts were observed more frequently in model tissues with low diffusion capacity, supporting this hypothesis.

The formation mechanism of the insoluble salt layer is depicted in figure 14. Body fluids maintain a pH of approximately 7.4 due to their buffering capacity [16]. Thus, if the diffusion rate in the tissue is sufficiently large compared to the corrosion rate of Mg, the concentrations of Mg^{2+} and OH^- will not increase. However, inadequate diffusion within the structure may lead to the precipitation of $Mg(OH)_2$. Conversely, if sufficient diffusion is maintained, Mg carbonate can be a primary insoluble salt formed on the specimen surface as Mg corrodes. This suppresses Mg corrosion, facilitating the recovery of pH closer to 7.4, resulting in the precipitation of phosphates. As indicated in table 9, Ca^{2+} exhibits lower solubility limits for carbonates and phosphates than Mg^{2+}. Interestingly, Ca^{2+} concentration in the body fluid surpasses the solubility limit for phosphate (supersaturated). The quantity of precipitated Ca phosphate is anticipated to rise in the shallow layers due to the decline in released Mg^{2+} caused by decreasing corrosion rates and local concentrations, a consequence of diffusion in the tissue.

5. Conclusion

In the present study, we performed immersion studies of pure Mg samples into model tissue with different thickener concentrations, and analyzed gas cavity formation and insoluble salt precipitation behavior. Obtained data confirmed that differences in diffusion environment influenced the precipitation of insoluble salt include Ca carbonate and phosphate through the differences in local OH^- and Mg^{2+} concentrations. Furthermore, the difference in diffusion ability also influenced the gas cavity formation in the tissue and Mg corrosion behavior. This implies that the implantation of Mg device into the tissue with low blood flow (low diffusion rate) causes gas cavity formation in the tissue, thereby inhibition of the precipitation of Ca salts. This finding on the influence of the tissue diffusion rate is only observed with *in vitro* experiment, that requires comparative evaluation by *in vivo* implantation, which we pan it in near future.

Data availability statement

All data that support the findings of this study are included within the article (and any supplementary files).

Acknowledgments

Part of this research was supported by Grants-in-Aid for Scientific Research (Issue Numbers 20K18407 and 22H03988) from the Japan Society for the Promotion of Science, and the 2022 TIA Collaboration Program Search and Promotion Project 'Kakehashi' (Serial Number TK22-015). We thank Ms Miho Oikawa of the Technical Division of Tohoku University Graduate School of Dentistry, Ms Yoko Nakano and Mr Syunsuke Kayamori of the Technical Division of Tohoku University Graduate School of Engineering, and Ms Akemi Kikuta of the National Institute for Materials and Science for their technical support.

ORCID iDs

Masanobu Hayashi https://orcid.org/0009-0009-0501-3234
Takayuki Aizawa https://orcid.org/0000-0002-6231-0368
Yoshimichi Imai https://orcid.org/0000-0001-5360-958X

References

[1] Chen Q and Thouas G A 2015 Metallic implant biomaterials *Mater. Sci. Eng. R. Rep.* **87** 1–57

[2] Niinomi M, Nakai M and Hieda J 2012 Development of new metallic alloys for biomedical applications *Acta Biomater.* **8** 3888–903

[3] van Bakelen N B, Boermans B D A, Buijs G J, Jansma J, Pruim G J, Hoppenreijs T J M, Bergsma J E, Stegenga B and Bos R R M 2014 Comparison of the long-term skeletal stability between a biodegradable and a titanium fixation system following BSSO advancement—a cohort study based on a multicenter randomised controlled trial *Br. J. Oral Maxillofac. Surg.* **52** 721–8

[4] Gareb B, van Bakelen N B, Dijkstra P U, Vissink A, Bos R R M and van Minnen B 2021 Efficacy and morbidity of biodegradable versus titanium osteosyntheses in orthognathic surgery: a systematic review with meta-analysis and trial sequential analysis *Eur. J. Oral Sci.* **129** e12800

[5] Ngo H X *et al* 2022 A narrative review of u-HA/PLLA, a bioactive resorbable reconstruction material: applications in oral and maxillofacial surgery *Materials* **15** 150

[6] Chen Y, Xu Z, Smith C and Sankar J 2014 Recent advances on the development of magnesium alloys for biodegradable implants *Acta Biomater.* **10** 4561–73

[7] Meier R and Panzica M 2017 Initial results with a resorbable MgYREZr compression screw in unstable scaphoid fractures show massive cyst formation *Handchir Mikrochir. Plast. Chir.* **49** 37–41

[8] Willbold E *et al* 2013 Biocompatibility of rapidly solidified magnesium alloy RS66 as a temporary biodegradable metal *Acta Biomater.* **9** 8509–17

[9] Zhao D, Witte F, Lu F, Wang J, Li J and Qin L 2017 Current status on clinical applications of magnesium-based orthopaedic implants: a review from clinical translational perspective *Biomaterials* **112** 287–302

[10] Miura C *et al* 2016 *In vivo* corrosion behaviour of magnesium alloy in association with surrounding tissue response in rats *Biomed. Mater.* **11** 025001

[11] Wang J, Giridharan V, Shanov V, Xu Z, Collins B, White L, Jang Y, Sankar J, Huang N and Yun Y 2014 Flow-induced corrosion behavior of absorbable magnesium-based stents *Acta Biomater.* **10** 5213–23

[12] Hafeez M A, Farooq A, Zang A, Saleem A and Deen K M 2020 Phosphate chemical conversion coatings for magnesium alloys: a review *J. Coat. Technol. Res.* **17** 827–49

[13] Hino M 2013 Pretreatment of magnesium alloys *J. Surf. Finish. Soc. Japan* **64** 650

[14] Yamamoto A and Kikuta A 2022 Development of a model system for gas cavity formation behavior of magnesium alloy implantation *ACS Biomater. Sci. Eng.* **8** 2437–44

[15] Amukarimi S and Mozafari M 2022 Biodegradable magnesium biomaterials—road to the clinic *Bioengineering* **9** 107

[16] Proksch E 2018 pH in nature, humans and skin *J. Dermatol.* **45** 1044–52

[17] Yamamoto A and Hiromoto S 2009 Effect of inorganic salts, amino acids and proteins on the degradation of pure magnesium *in vitro Mater. Sci. Eng.* C **29** 1559–68

[18] Gelli R, Briccolani-Bandini L, Pagliai M, Cardini G, Ridi F and Baglioni P 2022 Exploring the effect of Mg^{2+} substitution on amorphous calcium phosphate nanoparticles *J. Colloid Interface Sci.* **606** 444–53

[19] Yu M, Wang L, Zhang W and Ganss B 2019 An evolutionarily conserved subdomain in amelotin promotes amorphous calcium phosphate-to-hydroxyapatite phase transition *Cryst. Growth Des.* **19** 2104–13

[20] Stammeier J A, Purgstaller B, Hippler D, Mavromatis V and Dietzel M 2018 *In-situ* Raman spectroscopy of amorphous calcium phosphate to crystalline hydroxyapatite transformation *MethodsX* **5** 1241–50

[21] Karampas I A and Kontoyannis C G 2013 Characterization of calcium phosphates mixtures *Vib. Spectrosc.* **64** 126–33

[22] Schmid T, Kraft R and Dariz P 2021 Shedding light onto the spectra of lime—part 2: Raman spectra of Ca and Mg carbonates and the role of d-block element luminescence *J. Raman Spectrosc.* **52** 1462–72

[23] Schmid T and Dariz P 2015 Shedding light onto the spectra of lime: Raman and luminescence bands of CaO, $Ca(OH)_2$ and $CaCO_3$ *J. Raman Spectrosc.* **46** 141–6

[24] Kuenzel C, Zhang F, Ferrandiz-Mas V, Cheeseman C R and Gartner E M 2018 The mechanism of hydration of MgO-hydromagnesite blends *Cem. Concr. Res.* **103** 123–9

[25] Wang M, Cai Y, Zhao B and Zhu P 2017 Time-resolved study of nanomorphology and nanomechanic change of early-stage mineralized electrospun poly(lactic acid) fiber by scanning electron microscopy, Raman spectroscopy and atomic force microscopy *Nanomaterials* **7** 223

[26] Rygula A, Majzner K, Marzec K M, Kaczor A, Pilarczyk M and Baranska M 2013 Raman spectroscopy of proteins: a review *J. Raman Spectrosc.* **44** 1061–76

[27] RSoniya S and Nair V M 2016 Synthesis and characterization of nanostructured $Mg(OH)_2$ and MgO *Int. J. Sci. Res.* **5** 197–203

[28] Yan W, Lian Y-J, Zhang Z-Y, Zeng M-Q, Zhang Z-Q, Yin Z-Z, Cui L-Y and Zeng R-C 2020 *In vitro* degradation of pure magnesium—the synergetic influences of glucose and albumin *Bioact. Mater.* **5** 318–33

[29] Chen L, Blawert C, Yang J, Hou R, Wang X, Zheludkevich M L and Li W 2020 The stress corrosion cracking behaviour of biomedical Mg-1Zn alloy in synthetic or natural biological media *Corros. Sci.* **175** 108876

[30] Yamamoto A *et al* 2022 Metallic biomaterials ‘from basics to recent topics’ *Proc. 44th Japanese Society for Biomaterials* p 376